15 Valley-Spin Physics in 2D Semiconducting Transition Metal Dichalcogenides

Hongyi Yu and Wang Yao

15.1 Introduction

Monolayer group-VIB transition metal dichalcogenides (TMDs) have recently emerged as a new class of semiconductors with appealing properties. The compounds have the chemical composition of MX_2, where M stands for the transition metal element Mo or W, and X for the chalcogen element S or Se. The bulk crystals of the group-VIB TMDs are of the layered structures where the elementary unit, i.e. monolayer, is an X–M–X covalently bonded quasi-2D hexagonal lattice [1]. The monolayers are loosely bound together by the weak van der Waals force to form the bulk crystals. Monolayer TMDs can be extracted from bulk crystals by mechanical exfoliation [2–4], or synthesized using chemical vapor deposition or molecular beam epitaxy [5–10]. When TMDs are thinned down to the monolayer, the band gap crosses from an indirect one to the direct one [2, 3, 6, 11, 12], which is in the visible frequency range. The conduction and valence band edges in the monolayers are both located at the corners of the hexagonal Brillouin zone (BZ), i.e., the $\mathbf{K}$ and $-\mathbf{K}$ points that are related by time reversal. The two degenerate but inequivalent band extrema constitute a discrete index for low-energy electrons and holes, known as the valley pseudospin. Similar to the use of spin in spintronics, this valley pseudospin of carriers may be utilized to encode information in electronic devices, which has led to the concept of valley-based electronics (or valleytronics) that has been explored in various materials with multivalley band structures [13–22].

Monolayer TMDs have provided a remarkable new laboratory for the exploration of valley physics and valleytronic applications. Key to the utilization of carriers' internal quantum degree of freedom for information processing is the capability to distinguish between states that represent different pieces of information and to control the dynamics in the Hilbert space spanned by these states. This requires the internal quantum degree of freedom to be associated with measurable physical properties, allowing it to be coupled to external perturbations for measurement and control. In the 2D hexagonal crystals, it was shown earlier using graphene models that, when inversion symmetry is broken, the two degenerate valleys can be distinguished by pseudovector quantities, such as the Berry curvature and the magnetic moment, which must take opposite values at the time-reversal pair of valleys [15, 16]. The valley contrasted Berry curvatures and magnetic moments can couple to external electric and magnetic fields, respectively,

giving rise to the valley Hall effect and valley Zeeman effect. Because of the inversion symmetry breaking, optical interband transitions at the time reversal pair of valleys can also acquire valley-dependent transition selection rules. These valley-dependent phenomena make possible the manipulation of valley pseudospin via electric, magnetic, and optical means, and they have all been discovered in monolayer TMDs where the lattice has structural inversion asymmetry. Moreover, the strong spin–orbit coupling from the transition metal elements gives rise to an effective interaction between the valley pseudospin and the spin, making possible the interplay between these two degrees of freedom, and allowing spin manipulations via the valley phenomena.

In this chapter, we give an overview of the valley and spin physics in monolayer TMDs. The content is organized as follows. Section 15.2 briefly introduces the valley-dependent electronic structures at the band edges. Section 15.3 presents the various valley and spin-dependent phenomena in monolayer TMDs, including the valley and spin optical selection rules, the valley Zeeman effect, the valley and spin Hall effects, and the non-linear valley and spin currents from triogonal warping. In Section 15.4, we explain how the monolayer valley and spin physics can be inherited in bilayers. Our emphasis is on the basic physics and theoretical framework, while more details on the related experimental discoveries have been covered in other chapters of this collection.

15.2   Electronic Structure at the Band Edges

Figures 15.1(a) and (b) illustrate the quasi-2D hexagonal lattice of a TMD monolayer [1]. The M atom is coordinated by the six neighboring X atoms in a trigonal prismatic geometry. With the trigonal prismatic coordination, the structural inversion symmetry is broken in the monolayer, key to the emergence of the valley-dependent physics discussed here. There is mirror symmetry in the out-of-plane (z) direction, which, together with the time reversal symmetry, dictates an effective form of the coupling between the valley and the spin degrees of freedom.

First-principles calculations have found that the band edge Bloch wave functions near the conduction band minimum (valence band maximum) at $\pm\mathbf{K}$ are predominantly from the M $d_{z^2}\left(d_{x^2-y^2} \pm id_{xy}\right)$ orbital which is the eigenstate of the angular momentum operator $\hat{L}_z$ with magnetic quantum number $m = 0\,(m = \pm2)$ [23], plus a small contribution from the X p_x and p_y orbitals [1, 24] (Fig. 15.1(d)). The $\pm\mathbf{K}$ points are high-symmetry points invariant under the C_3 operation ($2\pi/3$ in-plane rotation). Thus the Bloch functions at $\pm\mathbf{K}$ are the eigenstates of C_3 with the eigenvalues $e^{i\frac{2}{3}l\pi}$, where l is an integer that depends on the choice of the rotation center (M, X, or h the hollow center of the hexagon formed by M and X, see Fig. 15.1(a)) [1]. In Table 15.1, the orbital contributions and the quantum number l are given for the conduction and valence band edge Bloch functions at the $\mathbf{K}$ point, while their counterparts at the $-\mathbf{K}$ point can be obtained by taking time reversal. The C_3 rotational symmetry, of the band edge Bloch functions, b underlies the valley optical selection rule in the monolayer and the interlayer hopping properties in the bilayer, to be discussed in the following sections.

Table 15.1 Rotational symmetry and orbital compositions of conduction and valence band Bloch functions at K point in monolayer *TMDs.* The Bloch functions are eigenstates of the C_3 rotation with eigenvalue $e^{i\frac{2}{3}l\pi}$, where l depends on the choice of rotation center that can be an M or X site, or the hollow center h of the M–X hexagon (Fig. 15.1(a)).

	M d	X p	l (M)	l (X)	l (h)
CBM	d_{z^2}	$p_x - ip_y$	0	+1	−1
VBM	$d_{x^2-y^2} + id_{xy}$	$p_x + ip_y$	+1	−1	0
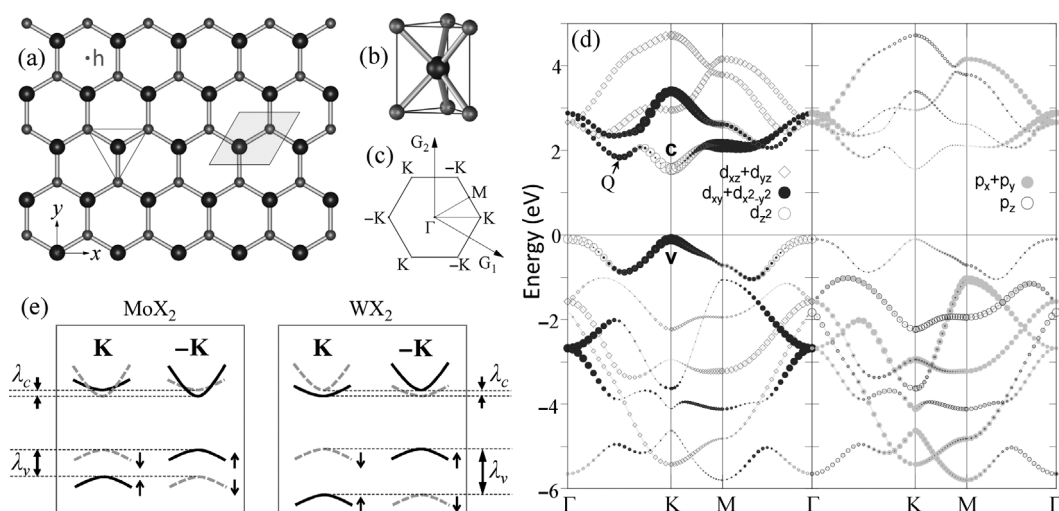
Fig. 15.1 (a) Monolayer group-VIB transition metal dichalcogenides from the top view. Large (small) spheres denote metal (chalcogen) atoms. (b) Trigonal prismatic coordination around a metal atom. The top view of this triangular prism is denoted by the triangle in (a). (c) The hexagonal first Brillouin zone, and the reciprocal lattice vectors G_1 and G_2. (d) Band structures of the MoS_2 monolayer from first-principles calculations without SOC, with the orbital composition illustrated. The metal d-orbitals and chalcogen p-orbitals are denoted by dots of different symbols, with the dot size proportional to the orbital weight in the corresponding state. (e) Schematics of the SOC splitting at the conduction and valence band edges at K and −K in MoX_2 and WX_2. Dashed gray (solid black) denotes the spin down (up) bands. ((a)–(c) Reproduced from [1] with permission from the Royal Society of Chemistry; (d) partly adapted with permission from [25]. Copyright 2013, American Physical Society.)

TMDs have a strong spin–orbit-coupling (SOC) originating from the M-d orbitals [1, 24, 26]. The form of the spin–orbit splitting at the band edges is dictated by the symmetries. With the mirror symmetry about the M-atom plane, the Bloch states in the monolayer are invariant under the mirror reflection operation. Considering the fact that mirror reflection of an in-plane spin vector is its opposite, while that of an out-of-plane spin vector is itself, the Bloch states must have their spin either parallel or antiparallel to the out-of-plane (z) direction, i.e. the SOC splitting must be in the z direction. Besides, time reversal symmetry requires the spin splitting to have opposite sign at an arbitrary

pair of momentum space points $\mathbf{k}$ and $-\mathbf{k}$. Thus in the neighborhood of $\mathbf{K}$ and $-\mathbf{K}$, the SOC manifests as an effective coupling between the spin component $\hat{S}_z$ ($=\pm 1/2$) and valley pseudospin component τ_z ($\tau_z = \pm 1$ for $\pm\mathbf{K}$ valley) [1, 24, 26]

$$\hat{H}_{\text{SOC}} = \lambda \tau_z \hat{S}_z. \tag{15.1}$$

First-principle calculations have found that the valence band at the $\mathbf{K}$ point has an SOC splitting of $\lambda_v \sim 0.15$ eV in the MoX_2 monolayer and $\lambda_v \sim 0.45$ eV in the WX_2 monolayer [24, 26–28]. Because of this giant SOC splitting, the valence band edge in monolayer TMDs has the spin index locked with the valley index, i.e. the $\mathbf{K}(-\mathbf{K})$ valley has only the spin up (down) low-energy holes, which are formed by removing spin down (up) valence electrons (Fig. 15.1(e)). Compared to the valence band edge from the $d_{x^2-y^2} \pm id_{xy}$ orbital that has a finite magnetic quantum number $m = \pm 2$, the conduction band edge is from the d_{z^2} orbital with $m = 0$. Thus the on-site spin–orbit coupling vanishes to the leading order. First-principles calculations find that the magnitude of conduction band spin splitting λ_c is a few meV for MoS_2 and tens of meV for $MoSe_2$, WS_2, and WSe_2 [24, 25, 29–37], which originates from the small X-p orbital compositions, as well as second-order effect mediated by the remote conduction band consisting of M-$d_{xz} \pm id_{yz}$ orbitals. The two contributions to SOC have opposite signs and their competition leads to the sign difference of λ_c between MoX_2 and WX_2 (Fig. 15.1(e)) [24, 25, 30].

The simplest theoretical model that gives a reasonably good description to the top valence band and lowest conduction bands is a three-band tight-binding model [25], constructed with the three M-d-orbitals only, i.e. d_{z^2} and $d_{x^2-y^2} \pm id_{xy}$, which are the major orbital compositions of the band edge Bloch functions in $\pm\mathbf{K}$ valleys. Including the M–M nearest-neighbor hopping only, the three-band tight-binding model describes the dispersions and Berry curvatures of conduction and valence bands near the $\pm\mathbf{K}$ points [25]. By including up to the third-nearest-neighbor hopping, all three bands agree well with the first-principles ones in the entire BZ [25]. This model has been applied to the study of edge states in TMD nanoribbons [38], quantum dots formed by lateral confinement potential in the extended TMD monolayer [39], intercellular orbital magnetic moment [40, 41], magnetoelectronic and optical properties [42], and magnetoluminescence [43].

Expanding the tight-binding model in the neighborhood of the $\pm\mathbf{K}$ points, the $\mathbf{k}\cdot\mathbf{p}$ model for describing the band edge physics can be obtained. By expanding the above three-band model and keeping to the linear order in $\mathbf{k}$, a minimum description of the conduction and valence band edges in $\tau_z\mathbf{K}$ valley has a rather simple form [26]

$$\hat{H}_{\mathbf{k}\cdot\mathbf{p}} = at\left(\tau_z k_x \hat{\sigma}_x + k_y \hat{\sigma}_y\right) + \frac{\Delta}{2}\hat{\sigma}_z - \lambda_v \tau_z \hat{S}_z. \tag{15.2}$$

Here $\hat{\sigma}_{x/y/z}$ is the Pauli matrix spanned by the conduction and valence states at the $\tau_z\mathbf{K}$ point, $\hat{S}_z$ is the Pauli matrix for spin, a is the lattice constant, t is the effective hopping integral, $\mathbf{k}$ is the wavevector measured from $\tau_z\mathbf{K}$, and λ_v is the valence band SOC splitting. This two-band $\mathbf{k}\cdot\mathbf{p}$ model is in fact the massive Dirac fermion model,

which captures the low-energy electronic structures in the $\pm\mathbf{K}$ valleys of monolayer TMDs, including the band dispersion, the Berry curvatures, and the giant SOC splitting of the valence band. The τ_z terms explicitly account for the valley dependence of the electronic structures at the band edges, which lead to the valley Hall effect, valley magnetic moment, and the valley-dependent optical selection rule which will be discussed in the following sections.

The two-band $\mathbf{k}\cdot\mathbf{p}$ model has been widely used to study various properties of TMD monolayers because of its simplicity. In the meantime, the simplicity of this model inevitably imposes some limitations on its applications. For example, it cannot account for the electron–hole asymmetry and the trigonal warping of band dispersion. The two effects can be accounted for by including terms quadratic in $\mathbf{k}$ [24, 25, 29, 44]. The corrected models with high-order terms have been used to study optical conductivity [45], magneto-optical properties [46], plasmons [47], and spin relaxation [48]. The small conduction band spin splitting at $\pm\mathbf{K}$, absent in the three-band tight-binding model and hence its $\mathbf{k}\cdot\mathbf{p}$ expansion, can also be added as a correction to Eq. (15.2) if needed.

15.3 Valley-Spin Physics in Monolayers

15.3.1 Valley and Spin Optical Selection Rules

The optical selection rules for interband transitions at $\pm\mathbf{K}$ points are the direct consequence of the C_3 rotational symmetry of Bloch functions discussed earlier (cf. Table 15.1) [1, 26, 49]. The interband optical transition matrix element satisfies

$$\langle\psi_{\mathrm{v},\pm\mathbf{K}}|\hat{P}_\pm|\psi_{\mathrm{c},\pm\mathbf{K}}\rangle = \langle C_3\psi_{\mathrm{v},\pm\mathbf{K}}|C_3\hat{P}_\pm C_3^{-1}|C_3\psi_{\mathrm{c},\pm\mathbf{K}}\rangle = e^{i\frac{2}{3}\pi(l_\mathrm{c}-l_\mathrm{v}\mp1)}\langle\psi_{\mathrm{v},\pm\mathbf{K}}|\hat{P}_\pm|\psi_{\mathrm{c},\pm\mathbf{K}}\rangle.$$

(15.3)

Here $\hat{P}_\pm \equiv \hat{P}_x \pm i\hat{P}_y$ is the momentum operator and $C_3\hat{P}_\pm C_3^{-1} = e^{\mp i\frac{2}{3}\pi}\hat{P}_\pm$. A finite $\langle\psi_{\mathrm{v},\pm\mathbf{K}}|\hat{P}_\pm|\psi_{\mathrm{c},\pm K}\rangle$ then requires $l_\mathrm{c} - l_\mathrm{v} \mp 1 = 3N$ with N being an integer. According to the l_c and l_v values summarized in Table 15.1, the interband optical transitions have the valley optical selection rules, i.e. coupled to the $\sigma^+(\sigma^-)$ polarized light only at $\mathbf{K}$ $(-\mathbf{K})$ [26] (Fig. 15.2(a)). Owing to the giant SOC splitting in the valence band, the valley optical selection rule also becomes a spin optical selection rule depending on the excitation frequency [26] (Fig. 15.2(a)). Optical excitations of electron–hole pairs with four distinct combinations of their spin and valley indices can be selectively realized through the choice of the polarization and frequency of the excitation light. In principle, such a selection rule is rigorous only at the high-symmetry $\pm\mathbf{K}$ points. Near the $\pm\mathbf{K}$ points, the $\mathbf{k}\cdot\mathbf{p}$ model in Eq. (15.2) leads to [26] $\left|\langle\psi_{\mathrm{v},\tau_z\mathbf{K}+\mathbf{k}}|\hat{P}_\pm|\psi_{\mathrm{c},\tau_z\mathbf{K}+\mathbf{k}}\rangle\right|^2 = m_e^2\frac{a^2t^2}{\hbar^2}(1\pm\tau_z\cos\theta)^2$, where $\theta = \arctan\left(\frac{2kat}{\Delta'}\right)$ and $\Delta' \equiv \Delta - \lambda_\mathrm{v}\tau_z S_z$. With the sizeable band gap Δ', the valley optical selection rule therefore holds in the neighborhood of $\pm\mathbf{K}$ points. First-principles calculations have also shown that the selection rule holds approximately true in a sufficiently large neighborhood of $\pm\mathbf{K}$ points [49].
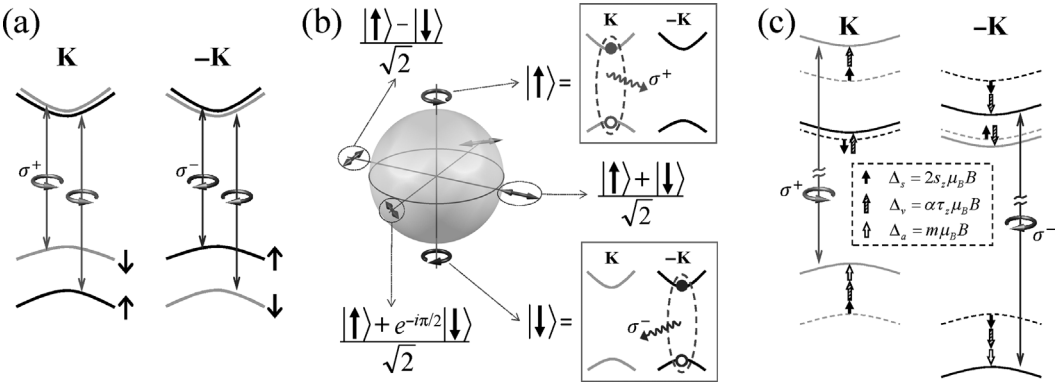
Fig. 15.2 (a) Valley and spin optical transition selection rules. (b) Optical orientation of excitonic valley pseudospin. A bright exciton in the K valley corresponds to valley pseudospin up ($\tau_z = +1$, north pole on the Bloch sphere), which couples exclusively to σ^+ circularly polarized photon, while bright exciton in the –K valley corresponds to valley pseudospin down ($\tau_z = -1$, south pole on the Bloch sphere), which couples to σ^- circularly polarized photon. The Bloch sphere equator corresponds to an equal superposition of the two valleys (in-plane valley pseudospin), which couples to linearly polarized photon with the polarization indicated by double arrows (reproduced from [50] with permission from Oxford University Press). (c) Valley-dependent Zeeman shifts of the band edges, from three contributions: solid black arrows denote the spin contribution, shaded for the Berry phase contribution, empty for the atomic orbital contribution. See text for explanation. The dashed (solid) curves are the bands under zero (finite) magnetic field. (Adapted from [41]. Copyright 2014, Nature Publishing Group.)

15.3.2   Optical Orientation of Excitonic Valley Pseudospin

Through the interband transition, the absorption of a photon excites a valence electron to the conduction band, leaving a vacancy in the filled valence band that is effectively described as a hole. The attractive Coulomb interaction between the negatively charged electron and the positively charged hole leads to their binding into a hydrogen-like bound pair, known as the exciton. Exciton plays a key role in optoelectronic phenomena in monolayer TMDs [50]. It can capture an extra electron or hole to form a negatively or positively charged exciton, also known as trion. The measured trion binding energy, i.e. the difference between the exciton and trion resonances in the absorption or photoluminescence, is of the order of tens of meV, about one order of magnitude larger than that in GaAs quantum wells. This points to an exceptionally large exciton binding energy of the order of hundreds of meV [51–54], which is also predicted by first-principles calculations [28, 33, 55–58], and jointly revealed by various measurements including the reflection spectra [59], two-photon absorption [60–63], and scanning tunneling microscopy/spectroscopy [10, 64–66]. Such strong Coulomb binding is due to the large effective masses of both electron and hole and the reduced dielectric screening in the 2D geometry [56, 59, 61, 67]. Meanwhile, the exciton wave function is largely the Wannier type, with electron and hole both well localized near the $\pm$**K** points in the momentum space [56, 61]. An exciton can then be classified by the valley

configuration of its electron and hole constituents. Due to the momentum conservation, the bright exciton that can radiatively recombine must have its electron and hole in the same valley. The two degenerate valley configurations of bright excitons can then be described by the excitonic valley pseudospin $\boldsymbol{\tau}$, where $\tau_z = +1$ and $\tau_z = -1$ correspond, respectively, to the exciton being in the $\mathbf{K}$ and $-\mathbf{K}$ valley (Fig. 15.2(b)).

These bright excitons inherit the valley optical selection rules of the band-to-band transitions at $\pm\mathbf{K}$ points, allowing their valley specific interconversion with photons of selected helicity: exciton with valley pseudospin up (down) $\tau_z = +1(-1)$ can be interconverted with a $\sigma^+(\sigma^-)$ circularly polarized photon (Fig. 15.2(b)). A linearly polarized photon is a coherent superposition of a σ^+ polarized photon and a σ^- polarized one, which can then interconvert with an exciton in a coherent superposition of being in the $\mathbf{K}$ and $-\mathbf{K}$ valley, transferring the optical coherence to valley quantum coherence [51]. Such a bright exciton carries an in-plane valley pseudospin, i.e. on the equator of the Bloch sphere representation of the excitonic valley pseudospin (Fig. 15.2(b)). Different points on the equator then correspond to photon linear polarization along different axis in the monolayer plane. The correspondence between the valley polarization/coherence and the photon polarization has been exploited for optical orientation of the excitonic valley pseudospin using circularly or linearly polarized excitation, as demonstrated in experiments of polarization-resolved photoluminesence [49, 51, 68–72]. The valley selective exciton–photon coupling has also enabled the pump–probe study of valley dynamics [73–77], and the valley selective optical Stark effect [78, 79] at different monolayer TMDs.

15.3.3   Valley Magnetic Moment and Valley Zeeman Effect

The magnetic moment of a Bloch electron characterizes its response to the magnetic field. In monolayer TMDs, the time reversal symmetry between $\mathbf{K}$ and $-\mathbf{K}$ requires their magnetic moment to have identical magnitude but opposite signs. An out-of-plane magnetic field then lifts the valley degeneracy, leading to a valley Zeeman effect. For the spin–valley locked band edges, the overall valley Zeeman shift has three contributions [40, 41, 80, 81] (Fig. 15.2(c)). The first is from the spin magnetic moment. The second is the atomic orbital magnetic moment. In monolayer TMDs, the conduction (valence) band in the $\pm\mathbf{K}$ valley mainly consists of M-$d_{z^2}\left(d_{x^2-y^2} \pm id_{xy}\right)$ orbitals with the magnetic quantum $m = 0$ ($m = \pm2$). This contributes to a Zeeman shift of 0 and $\pm2\mu_B B$ for the conduction and valence band, respectively. The third is a lattice contribution (i.e. vanishes when the hopping between the lattice sites is turned off), which is also associated with the Berry phase effect of the Bloch electrons [82]. This lattice contribution is given by [16, 83]

$$\mathbf{m}_{n,\mathbf{k}} = -i\frac{e\hbar}{2m^2} \sum_{i\neq n} \frac{\langle u_{n,\mathbf{k}}|\hat{\mathbf{p}}|u_{i,\mathbf{k}}\rangle \times \langle u_{i,\mathbf{k}}|\hat{\mathbf{p}}|u_{n,\mathbf{k}}\rangle}{E_{n,\mathbf{k}} - E_{i,\mathbf{k}}}, \tag{15.4}$$

where $u_{n,\mathbf{k}}$ is the periodic part of the Bloch function of the nth band at wavevector $\mathbf{k}$, and $E_{n,\mathbf{k}}$ is the band dispersion.

The valley Zeeman shift of the conduction and valence band edges can manifest in the energy cost of generating an electron–hole pair in a specific valley, so the two valley bright exciton states will also have a valley Zeeman splitting, making possible magneto-control of the excitonic valley pseudospin dynamics. With the valley optical selection rule, the exciton valley Zeeman splitting may be detected from the polarization-resolved PL measurement, where the magnetic field is expected to shift in opposite directions with the σ^+ and σ^- polarized PL peaks that correspond to the bright exciton resonances in valley $\mathbf{K}$ and $-\mathbf{K}$, respectively [40, 41, 80, 81] (Fig. 15.2(c)). The exciton valley Zeeman splitting measures the difference between the Zeeman shifts of the conduction and valence band edges, so the three contributions to the magnetic moment of the spin–valley locked band edge carriers are partially inherited. Firstly, the spin magnetic moment does not affect the optical resonances, because optical transitions conserve spin so that the shift of the initial and final states due to the spin magnetic moment is identical. Secondly, with the conduction (valence) band in the $\pm\mathbf{K}$ valley mainly consisting of M-d_{z^2} $\left(d_{x^2-y^2} \pm i d_{xy}\right)$ orbitals with the magnetic quantum $m = 0$ $(m = \pm 2)$, the magnetic moment of the atomic orbital is a major contribution to the valley Zeeman shift of the exciton resonance (Fig. 15.2(c)). Lastly, we note the lattice contribution to the magnetic moment also results in a finite exciton valley Zeeman shift. Within the minimum two-band massive Dirac fermion model of Eq. (15.2), the electron and hole magnetic moment associated with the Berry phase effect exactly cancel because of the particle–hole symmetry. Nevertheless, corrections beyond the two-band model result in a finite difference for the electron and hole magnetic moment, and it is this difference, as well as the atomic orbital contribution, that is measured by the splitting of the σ^+ and σ^- PL peaks [40, 41].

15.3.4   Berry Phase Effect and Valley Hall Current

The Berry phase effect for a particle lies in the dependence of the internal structure on the dynamical parameter [82]. In the context of Bloch electrons, it lies in the dependence of the periodic part of the Bloch function $u_{n,\mathbf{k}}$ on the wavevector $\mathbf{k}$. Consider a wavepacket of Bloch electrons moving adiabatically in a non-degenerate energy band with band index n. Under smooth perturbations, it is possible to construct the wave-packet with a length scale that is small compared to that of the external perturbation but large compared to the lattice constant. One can then speak simultaneously of the central position of the electron in real and in momentum space, and the semiclassical equation of motion for the Bloch electron is then written [15, 83]

$$\dot{\mathbf{r}} = \frac{1}{\hbar}\frac{\partial E_{n,\mathbf{k}}}{\partial \mathbf{k}} - \dot{\mathbf{k}} \times \boldsymbol{\Omega}_{n,\mathbf{k}}, \hbar\dot{\mathbf{k}} = -e\mathbf{E} - e\dot{\mathbf{r}} \times \mathbf{B}, \tag{15.5}$$

$\boldsymbol{\Omega}$ is a pseudovector that captures the Berry phase effect in the Bloch band, known as the *Berry curvature* [16, 83]

$$\boldsymbol{\Omega}_{n,\mathbf{k}} = i\frac{\hbar^2}{m^2}\sum_{i \neq n}\frac{\langle u_{n,\mathbf{k}}|\hat{\mathbf{p}}|u_{i,\mathbf{k}}\rangle \times \langle u_{i,\mathbf{k}}|\hat{\mathbf{p}}|u_{n,\mathbf{k}}\rangle}{\left(E_{n,\mathbf{k}} - E_{i,\mathbf{k}}\right)^2}. \tag{15.6}$$

Obviously, in an applied electric field the $\mathbf{\Omega}$ term corresponds to an anomalous velocity perpendicular to the field, i.e. a Hall effect. The Berry curvature has a form similar to the lattice contribution of the magnetic moment $\mathbf{m}$ (cf. Eq. (15.4)), so non-zero Berry curvature in general implies a finite magnetic moment, and vice versa.

In monolayer TMDs, the $\pm\mathbf{K}$ valley conduction and valence bands can be described by the massive Dirac fermion model, which together with the inversion symmetry breaking give rise to sizeable Berry curvatures with opposite signs at the two valleys [15, 16, 26]

$$\Omega_{\mathbf{v},\mathbf{k}} = -\Omega_{\mathbf{c},\mathbf{k}} = \tau_z \frac{2a^2t^2\Delta'}{\left(\Delta'^2 + 4a^2t^2k^2\right)^{3/2}}, \quad \Delta' \equiv \Delta - \lambda_{\mathrm{v}}\tau_z S_z. \tag{15.7}$$

In the presence of an in-plane electric field, the valley contrasting $\mathbf{\Omega}$ gives rise to a Hall current of the carriers with the sign depending on the valley index [16, 26, 84] (Figs. 15.3(a) and (b)), i.e. a *valley Hall* effect. The valley Hall effect is an analog of the spin Hall effect [85–87], but with the valley pseudospin playing the role of spin. For hole doped systems, because the spin index is locked with the valley index for the band edge holes, the valley Hall effect is at the same time a spin Hall effect (Fig. 15.3(a)). For n-doped monolayers, the finite conduction band spin splitting can lead to different populations of spin up and down electrons in a given valley (cf. Fig. 15.1(e)), and the spin dependence of Δ' in Eq. (15.7) also results in different magnitudes of their Berry curvatures. As a result, the valley Hall effect of electrons is also accompanied by the spin Hall effect (Fig. 15.3(b)). Passing a longitudinal current through the monolayer, the valley Hall effect in the 2D bulk will lead to valley polarization on the edges, which can be detected from the Kerr rotation of an incident linearly polarized light based on the valley optical selection rules [88].

The valley contrasting Berry curvature and the valley optical selection rules together can further lead to a Hall effect that can be detected from electrical measurement [16]. Optical field with $\sigma^+(\sigma^-)$ circular polarization selectively excite electrons and holes in the $\mathbf{K}(-\mathbf{K})$ valley. Driven by an in-plane electric field, these photoexcited electrons
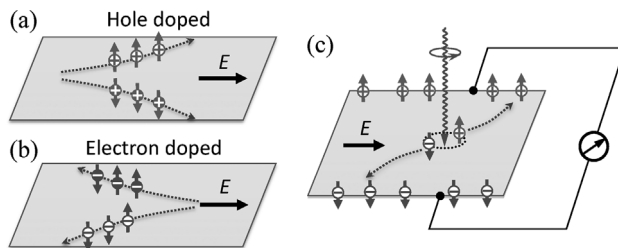
Fig. 15.3 (a) Valley Hall effect of holes in TMDs monolayers, which is a spin Hall effect at the same time because of the spin–valley locking of holes. (b) Valley Hall effect of electrons, also accompanied by a spin Hall effect (see text). (c) Valley Hall effect under the excitation by a circularly polarized light. The valley polarized electron and hole tend to move to the opposite edges, contributing with the same sign to the Hall voltage. (Adapted with permission from [26]. Copyright 2013, American Physical Society.)

and holes will acquire opposite transverse velocities because of the conduction and valence band Berry curvatures, which then move to the two opposite edges, contributing the same sign to the Hall voltage [16, 26] (Fig. 15.3(c)). Such Hall effects of photo injected carriers have already been observed in monolayer MoS_2 and WS_2 [89, 90].

15.3.5   Non-Linear Valley-Spin Current Response from Trigonal Warping

The valley Hall effect is a linear response to the electric field. The valley current in the transverse direction is always accompanied by the much larger longitudinal charge current, a major cause of dissipation that cannot be removed as it has the same linear dependence on the field. Here we show that there exists another mechanism for generating bulk valley current in monolayer TMDs, which is a quadratic response to the electric field that makes possible current rectification to generate dc valley currents by ac electric field, with the absence of net charge current. The effect arises from the trigonal warping of the band edges at the $\pm\mathbf{K}$ valleys, which corrects the parabolic dispersion to [29]

$$E_{\tau_z,\mathbf{k}} = \frac{\hbar^2 k^2}{2m^*}(1 + \tau_z \beta k \cos 3\theta). \tag{15.8}$$

Here $\mathbf{k} \equiv (k\cos\theta, k\sin\theta)$ is the wavevector measured from the band edge $\tau_z\mathbf{K}$ point, m^* is the effective mass, and β characterizes the degree of warping. The valley index τ_z in the trigonal warping term ensures the time reversal symmetry between the $\mathbf{K}$ and $-\mathbf{K}$ valleys, which have opposite trigonal warping (see Figs. 15.4(a) and (b)). The trigonal warping term couples the valley index to the momentum, so the current response to an in-plane electric field becomes valley dependent. This gives rise to a finite valley current $\mathbf{j}_v$, defined as the difference between the current responses in the two valleys [91]. For the spin–valley locked band edge carriers in monolayer TMDs, the valley current is also a spin current.

Under the relaxation time approximation and in the limit of weak intervalley scattering, such valley current arises in the second order of the applied electric field [91]

$$\mathbf{j}_v \propto \beta|\mathbf{k}_d|^2(\cos 2\theta_E, -\sin 2\theta_E). \tag{15.9}$$

Here $\mathbf{k}_d = e\tau_p\mathbf{E}/\hbar$ is the Fermi surface displacement under the electric field $\mathbf{E} \equiv (E\cos\theta_E, E\sin\theta_E)$, with θ_E the angle between the field direction and the zig-zag crystalline axis, and τ_p the momentum relaxation time. Figure 15.4(c) shows the angle dependence of the valley current direction on both the field direction and the crystalline axis. For $\mathbf{E}$ in the zig-zag (armchair) direction, the non-linear valley current is along (perpendicular to) the field (see Figs. 15.4(a) and (b)). In an ac electric field, the dc charge current is absent, while there is a dc valley current, as the valley currents in opposite electric fields point in the same direction (Fig. 15.4(c)). From the quadratic dependence of $\mathbf{j}_v$ on $\mathbf{k}_d$ in Eq. (15.9), it is clear that the non-linear valley current favors large mobility. Taking a mobility value of ~1000 cm^2 V^{-1} s^{-1} that has been achieved at low temperature [92, 93], we estimate the non-linear valley current magnitude starts to exceed that of the valley Hall current at an electric field of ~10 mV μm^{-1}.
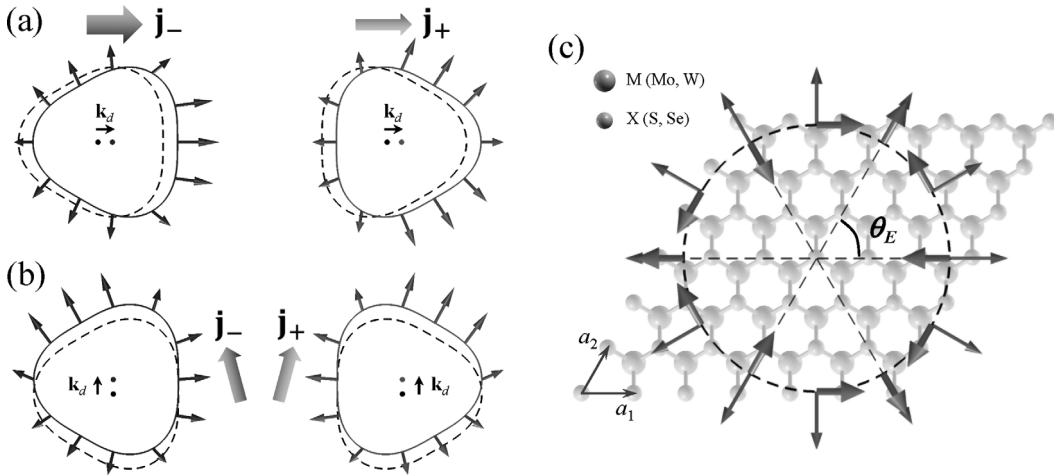
Fig. 15.4 (a) Displacements of Fermi pockets at K (right) and –**K** (left) by an electric field along the zig-zag direction. The thick arrow on top marked as j_+ (j_-) denotes the current from the Fermi pocket **K** (−**K**). The valley (spin) current $j_v \equiv j_+ - j_-$ is parallel to the field. The thin arrows illustrate the group velocity on the displaced **K** (−**K**) valley Fermi surface. (b) The electric field along the armchair direction. The valley (spin) current is perpendicular to the field. (c) The dependence of the spin/valley current direction (large arrow on the circle) on the relative angle θ_E between the field (small arrow on the circle) and the crystalline axis. (Adapted with permission from [91]. Copyright 2013, American Physical Society.)

We summarize here the key differences between the two mechanisms for bulk valley current generation. The origin of the non-linear valley current is valley-dependent dispersion, arising from the Fermi surface anisotropy for a time-reversal pair of valleys, while the valley Hall current is induced by the finite Berry curvatures of the carriers. The valley Hall effect requires inversion symmetry breaking, which is not necessary for the non-linear valley current studied here. The valley Hall current is always perpendicular to the electric field and is independent of the crystalline axis, while the direction of the non-linear valley current is determined by both the direction of the electric field and the crystalline axis.

15.4   Valley and Spin Physics in Bilayers

Natural crystals of the four TMDs of interest (MS_2 and MSe_2) are mostly the 2H stacked ones, where the adjacent monolayers are rotated 180° to each other, with M sites of one layer sitting right on top of the X sites of the adjacent layer. Figure 15.5(a) shows the unit cell of the 2H stacked bilayer and bulk, where inversion symmetry is restored. Albeit less stable than the 2H stacking, 3R is another possible stacking order for the bulk crystals of the four TMDs of interest. 3R stacking has the same monolayer unit as the 2H stacking, while the neighboring layers are simply translations of each other [94, 95] (Fig. 15.5(b)), so the inversion symmetry is still broken.
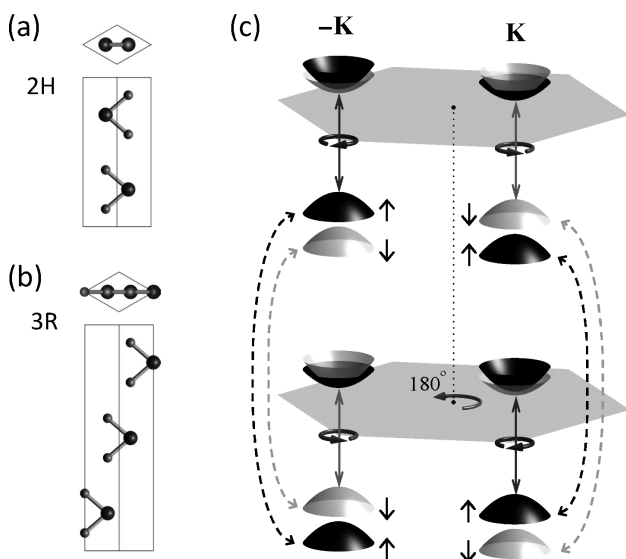
Fig. 15.5 (a) 2H stacking. Top and side views of a bulk unit cell. (b) 3R stacking. (c) Conduction and valence band edges of two WX_2 monolayers in 2H stacking, where the lower layer is the 180° rotation of the upper layer. The dashed double-headed arrows illustrate the spin-conserving interlayer hoppings. The hopping-induced layer hybridization is substantially quenched by the valley and layered-dependent giant spin splitting. ((a) Reproduced from [1] with permission from the Royal Society of Chemistry.)

The valley and spin physics of the monolayer is inherited in different ways in the 2H and 3R stacking. For the 3R stacking, the interlayer hopping simply vanishes at the $\pm\mathbf{K}$ points for both the conduction and valence bands, because of the rotational symmetry of the band edge Bloch functions. The hopping matrix element between two adjacent layers write

$$
\begin{aligned}
\langle\psi_{U,\pm\mathbf{K}}|\hat{H}_{int}|\psi_{L,\pm\mathbf{K}}\rangle &= \langle C_3\psi_{U,\pm\mathbf{K}}|C_3\hat{H}_{int}C_3^{-1}|C_3\psi_{L,\pm\mathbf{K}}\rangle \\
&= e^{i\frac{2}{3}\pi(l_U-l_L)}\langle\psi_{U,\pm\mathbf{K}}|\hat{H}_{int}|\psi_{L,\pm\mathbf{K}}\rangle.
\end{aligned}
\tag{15.10}
$$

A non-zero hopping matrix element therefore requires the two quantum numbers l_U and l_L to be identical. For the 3R stacking, an X-site in the upper layer sits on top of an M-site in the lower layer, which can be taken as the center of the in-plane C_3 rotations in Eq. (15.10). Thus, the values of l_U and l_L are to be taken, respectively, from the X and M columns in Table 15.1, which are different for either the conduction or the valence band edge Bloch functions. Thus the interlayer hopping vanishes at $\pm\mathbf{K}$ for both the conduction and valence bands. The optical selection rules and valley Hall effect of the monolayer are directly inherited in the 3R bilayer and multilayers [95].

For 2H stacking, similar analysis can show that the interlayer hopping vanishes at $\pm\mathbf{K}$ in the conduction band [1, 96, 97]. In the valence band, however, the interlayer hopping is finite at $\pm\mathbf{K}$, and its competition with the large spin–valley coupling has interesting consequences. Figure 15.5(c) schematically shows the band edges of two

monolayers in 2H stacking order, with dashed arrows illustrating the interlayer hopping that conserves the spin and momentum. The $180°$ rotation of the lower layer (relative to the upper layer) switches the $\pm\mathbf{K}$ valleys. As a result, the sign of the spin splitting becomes dependent on both the valley index and the layer index. Introducing pseudo-spin χ to denote the layer degree of freedom ($\chi_z = 1$ for upper, and $\chi_z = -1$ for lower layer), the holes at $\tau_z\mathbf{K}$ can be described by

$$\hat{H}_{2\mathrm{H}} = \lambda_\mathrm{v}\tau_z\hat{S}_z\chi_z + t_\perp\chi_x. \tag{15.11}$$

The first term characterizes the SOC, i.e. the valley and layered-dependent spin splitting, which manifests as an effective coupling between spin, valley, and layer pseudospins. The second term is the interlayer hopping, where first-principle calculations finds $t_\perp$ in the order of tens meV. The SOC strength λ_v then corresponds to the energy cost of the interlayer hopping.

In WX_2, where λ_v is much larger than $t_\perp$, interlayer hybridization is substantially quenched by the giant SOC splitting [1, 12, 98]. Thus in 2H bilayer WX_2, both the conduction and valence Bloch states in the $\pm\mathbf{K}$ valleys are predominantly localized in either the upper or the lower layer. The $\pm\mathbf{K}$ valley physics is essentially that of the two decoupled monolayers. The valley Hall currents from the two layers average out, but the spin Hall currents add constructively. Under excitation by circularly polarized light, e.g. σ^+, valley $-\mathbf{K}$ is excited in the upper layer while valley $\mathbf{K}$ is excited in the lower layer, so there is no net valley polarization generated. However, σ^+ excites spin up exclusively in both layers, so the spin optical selection rules are still present in the inversion symmetric bilayers. Circular polarized PL can now come from the spin optical selection rule and is not necessarily an indication of inversion symmetry.

In MoX_2, λ_v has comparable magnitude to $t_\perp$, so the layer hybridization becomes non-negligible. In such a case, an interlayer bias that breaks the inversion symmetry in the bilayer can substantially change the layer polarizations of the Bloch states in the $\pm\mathbf{K}$ valley, affecting the valley related phenomena. Experiments have shown that the degree of circular polarization of photoluminescence under a circularly polarized excitation can be continuously tuned between zero and finite as a function of gate voltage in bilayer MoS_2 [99]. The tuning of the valley Hall effect by interlayer bias in bilayer MoS_2 is also reported recently through the detection of valley polarization accumulated via the Kerr rotation measurements [88, 89]. These experiments indicate a controllable way to tune the valley physical properties by changing the symmetry of the system.

Lastly, it is worth noting a unique possibility of controlling the spin and pseudospins in 2H bilayers. With the effective coupling of spin and valley to the layer pseudospin, concerning the carriers in the lower energy spin-split subband, the spin index is now locked to the layer pseudospin polarization in a given valley. As the layer pseudospin couples to the electric field in the perpendicular direction, such spin-layer locking suggests the possibility of controlling these quantum degrees of freedom by various magnetoelectric effects [96, 97, 99]. For example, the electric field can now induce a spin splitting much larger than that possible in a magnetic field [96, 97], while in-plane magnetic field can induce charge oscillations between the layers [96].

15.5   References

[1] G.-B. Liu, D. Xiao, Y. Yao, X. Xu, and W. Yao, *Chem. Soc. Rev.* **44**, 2643 (2015).

[2] K. F. Mak, C. Lee, J. Hone, J. Shan, and T. F. Heinz, *Phys. Rev. Lett.* **105**, 136805 (2010).

[3] A. Splendiani, L. Sun, Y. Zhang, T. Li, J. Kim, C.-Y. Chim, G. Galli, and F. Wang, *Nano Lett.* **10**, 1271 (2010).

[4] K. S. Novoselov, D. Jiang, F. Schedin, T. J. Booth, V. V. Khotkevich, S. V. Morozov, and A. K. Geim, *Proc. Natl. Acad. Sci. USA* **102**, 10451 (2005).

[5] K.-K. Liu *et al.*, *Nano Lett.* **12**, 1538 (2012).

[6] Y. Zhang *et al.*, *Nature Nanotech.* **9**, 111 (2014).

[7] Y. Zhan, Z. Liu, S. Najmaei, P. M. Ajayan, and J. Lou, *Small* **8**, 966 (2012).

[8] A. M. v. d. Zande *et al.*, *Nature Mater.* **12**, 554 (2013).

[9] S. Najmaei *et al.*, *Nature Mater.* **12**, 754 (2013).

[10] H. Liu *et al.*, *Phys. Rev. Lett.* **113**, 066105 (2014).

[11] W. Jin *et al.*, *Phys. Rev. Lett.* **111**, 106801 (2013).

[12] H. Zeng *et al.*, *Sci. Rep.* **3**, 1608 (2013).

[13] O. Gunawan, Y. P. Shkolnikov, K. Vakili, T. Gokmen, E. P. D. Poortere, and M. Shayegan, *Phys. Rev. Lett.* **97**, 186404 (2006).

[14] A. Rycerz, J. Tworzydlo, and C. W. J. Beenakker, *Nature Phys.* **3**, 172 (2007).

[15] D. Xiao, W. Yao, and Q. Niu, *Phys. Rev. Lett.* **99**, 236809 (2007).

[16] W. Yao, D. Xiao, and Q. Niu, *Phys. Rev. B* **77**, 235406 (2008).

[17] N. C. Bishop, M. Padmanabhan, K. Vakili, Y. P. Shkolnikov, E. P. D. Poortere, and M. Shayegan, *Phys. Rev. Lett.* **98**, 266404 (2007).

[18] Y. P. Shkolnikov, E. P. D. Poortere, E. Tutuc, and M. Shayegan, *Phys. Rev. Lett.* **89**, 226805 (2002).

[19] K. Takashina, Y. Ono, A. Fujiwara, Y. Takahashi, and Y. Hirayama, *Phys. Rev. Lett.* **96**, 236801 (2006).

[20] J. Karch, S. A. Tarasenko, E. L. Ivchenko, J. Kamann, P. Olbrich, M. Utz, Z. D. Kvon, and S. D. Ganichev, *Phys. Rev. B* **83**, 121312 (2011).

[21] J. Isberg, M. Gabrysch, J. Hammersberg, S. Majdi, K. K. Kovi, and D. J. Twitchen, *Nature Mater.* **12**, 760 (2013).

[22] Z. Zhu, A. Collaudin, B. Fauqué, W. Kang, and K. Behnia, *Nature Phys.* **8**, 89 (2012).

[23] L. F. Mattheiss, *Phys. Rev. B* **8**, 3719 (1973).

[24] A. Kormányos, G. Burkard, M. Gmitra, J. Fabian, V. Zólyomi, N. D. Drummond, and V. Fal'ko, *2D Mater.* **2**, 022001 (2015).

[25] G.-B. Liu, W.-Y. Shan, Y. Yao, W. Yao, and D. Xiao, *Phys. Rev. B* **88**, 085433 (2013).

[26] D. Xiao, G.-B. Liu, W. Feng, X. Xu, and W. Yao, *Phys. Rev. Lett.* **108**, 196802 (2012).

[27] Z. Y. Zhu, Y. C. Cheng, and U. Schwingenschlögl, *Phys. Rev. B* **84**, 153402 (2011).

[28] A. Ramasubramaniam, *Phys. Rev. B* **86**, 115409 (2012).

[29] A. Kormányos, V. Zólyomi, N. D. Drummond, P. Rakyta, G. Burkard, and V. I. Fal'ko, *Phys. Rev. B* **88**, 045416 (2013).

[30] A. Kormányos, V. Zólyomi, N. D. Drummond, and G. Burkard, *Phys. Rev. X* **4**, 011034 (2014).

[31] K. Kośmider, J. W. González, and J. Fernández-Rossier, *Phys. Rev. B* **88**, 245436 (2013).

[32] E. S. Kadantsev and P. Hawrylak, *Solid State Commun.* **152**, 909 (2012).

[33] T. Cheiwchanchamnangij and W. R. L. Lambrecht, *Phys. Rev. B* **85**, 205302 (2012).

[34] K. Kośmider and J. Fernández-Rossier, *Phys. Rev. B* **87**, 075451 (2013).

[35] R. Roldán, M. P. López-Sancho, F. Guinea, E. Cappelluti, J. A. Silva-Guillén, and P. Ordejón, *2D Mater*. **1**, 034003 (2014).

[36] T. Cheiwchanchamnangij, W. R. L. Lambrecht, Y. Song, and H. Dery, *Phys. Rev. B* **88**, 155404 (2013).

[37] H. Ochoa and R. Roldán, *Phys. Rev. B* **87**, 245421 (2013).

[38] R.-L. Chu, G.-B. Liu, W. Yao, X. Xu, D. Xiao, and C. Zhang, *Phys. Rev. B* **89**, 155317 (2014).

[39] G.-B. Liu, H. Pang, Y. Yao, and W. Yao, *New J. Phys*. **16**, 105011 (2014).

[40] A. Srivastava, M. Sidler, A. V. Allain, D. S. Lembke, A. Kis, and A. Imamoğlu, *Nature Phys*. **11**, 141 (2015).

[41] G. Aivazian *et al.*, *Nature Phys*. **11**, 148 (2015).

[42] Y.-H. Ho, Y.-H. Wang, and H.-Y. Chen, *Phys. Rev. B* **89**, 155316 (2014).

[43] R.-L. Chu, X. Li, S. Wu, Q. Niu, W. Yao, X. Xu, and C. Zhang, *Phys. Rev. B* **90**, 045427 (2014).

[44] H. Rostami, A. G. Moghaddam, and R. Asgari, *Phys. Rev. B* **88**, 085440 (2013).

[45] H. Rostami and R. Asgari, *Phys. Rev. B* **89**, 115413 (2014).

[46] F. Rose, M. O. Goerbig, and F. Piéchon, *Phys. Rev. B* **88**, 125438 (2013).

[47] A. Scholz, T. Stauber, and J. Schliemann, *Phys. Rev. B* **88**, 035135 (2013).

[48] L. Wang and M. W. Wu, *Phys. Rev. B* **89**, 115302 (2014).

[49] T. Cao *et al.*, *Nat. Commun*. **3**, 887 (2012).

[50] H. Yu, X. Cui, X. Xu, and W. Yao, *Natl. Sci. Rev*. **2**, 57 (2015).

[51] A. M. Jones *et al.*, *Nature Nanotech*. **8**, 634 (2013).

[52] J. S. Ross *et al.*, *Nat. Commun*. **4**, 1474 (2012).

[53] K. F. Mak, K. He, C. Lee, G. H. Lee, J. Hone, T. F. Heinz, and J. Shan, *Nature Mater*. **12**, 207 (2012).

[54] A. A. Mitioglu, P. Plochocka, J. N. Jadczak, W. Escoffier, G. L. J. A. Rikken, L. Kulyuk, and D. K. Maude, *Phys. Rev. B* **88**, 245403 (2013).

[55] J. Feng, X. Qian, C.-W. Huang, and J. Li, *Nature Photon*. **6**, 866 (2012).

[56] D. Y. Qiu, F. H. d. Jornada, and S. G. Louie, *Phys. Rev. Lett*. **111**, 216805 (2013).

[57] H.-P. Komsa and A. V. Krasheninnikov, *Phys. Rev. B* **86**, 241201 (2012).

[58] H. Shi, H. Pan, Y.-W. Zhang, and B. I. Yakobson, *Phys. Rev. B* **87**, 155304 (2013).

[59] A. Chernikov, T. C. Berkelbach, H. M. Hill, A. Rigosi, Y. Li, O. B. Aslan, D. R. Reichman, M. S. Hybertsen, and T. F. Heinz, *Phys. Rev. Lett*. **113**, 076802 (2014).

[60] K. He, N. Kumar, L. Zhao, Z. Wang, K. F. Mak, H. Zhao, and J. Shan, *Phys. Rev. Lett*. **113**, 026803 (2014).

[61] Z. Ye, T. Cao, K. O'Brien, H. Zhu, X. Yin, Y. Wang, S. G. Louie, and X. Zhang, *Nature* **513**, 214 (2014).

[62] B. Zhu, X. Chen, and X. Cui, *Sci. Rep*. **5**, 9218 (2015).

[63] G. Wang, X. Marie, I. Gerber, T. Amand, D. Lagarde, L. Bouet, M. Vidal, A. Balocchi, and B. Urbaszek, *Phys. Rev. Lett*. **114**, 097403 (2015).

[64] C. Zhang, A. Johnson, C.-L. Hsu, L.-J. Li, and C.-K. Shih, *Nano Lett*. **14**, 2443 (2014).

[65] M. M. Ugeda *et al.*, *Nature Mater*. **13**, 1091 (2014).

[66] M.-H. Chiu *et al.*, *Nat. Commun*. **6**, 7666 (2015).

[67] T. C. Berkelbach, M. S. Hybertsen, and D. R. Reichman, *Phys. Rev. B* **88**, 045318 (2013).

[68] H. Zeng, J. Dai, W. Yao, D. Xiao, and X. Cui, *Nature Nanotech*. **7**, 490 (2012).

[69] K. F. Mak, K. He, J. Shan, and T. F. Heinz, *Nature Nanotech*. **7**, 494 (2012).

[70] G. Wang, M. M. Glazov, C. Robert, T. Amand, X. Marie, and B. Urbaszek, *Phys. Rev. Lett*. **115**, 117401 (2015).

[71] G. Sallen *et al.*, *Phys. Rev. B* **86**, 081301(R) (2012).

[72] G. Wang, L. Bouet, D. Lagarde, M. Vidal, A. Balocchi, T. Amand, X. Marie, and B. Urbaszek, *Phys. Rev. B* **90**, 075413 (2014).

[73] C. Mai, A. Barrette, Y. Yu, Y. G. Semenov, K. W. Kim, L. Cao, and K. Gundogdu, *Nano Lett*. **14**, 202 (2014).

[74] Q. Wang, S. Ge, X. Li, J. Qiu, Y. Ji, J. Feng, and D. Sun, *ACS Nano* **7**, 11087 (2013).

[75] J. R. Schaibley *et al.*, *Phys. Rev. Lett*. **114**, 137402 (2015).

[76] C. Mai, Y. G. Semenov, A. Barrette, Y. Yu, Z. Jin, L. Cao, K. W. Kim, and K. Gundogdu, *Phys. Rev. B* **90**, 041414 (2014).

[77] N. Kumar, J. He, D. He, Y. Wang, and H. Zhao, *Nanoscale* **6**, 12690 (2014).

[78] E. J. Sie, J. W. McIver, Y.-H. Lee, L. Fu, J. Kong, and N. Gedik, *Nature Mater*. **15**, 711 (2014).

[79] J. Kim, X. Hong, C. Jin, S.-F. Shi, C.-Y. S. Chang, M.-H. Chiu, L.-J. Li, and F. Wang, *Science* **346**, 1205 (2014).

[80] Y. Li *et al.*, *Phys. Rev. Lett*. **113**, 266804 (2014).

[81] D. MacNeill, C. Heikes, K. F. Mak, Z. Anderson, A. Kormányos, V. Zólyomi, J. Park, and D. C. Ralph, *Phys. Rev. Lett*. **114**, 037401 (2015).

[82] D. Xiao, M.-C. Chang, and Q. Niu, *Rev. Mod. Phys*. **82**, 1959 (2010).

[83] X. Xu, W. Yao, D. Xiao, and T. F. Heinz, *Nature Phys*. **10**, 343 (2014).

[84] H. Yu, G.-B. Liu, P. Gong, X. Xu, and W. Yao, *Nat. Commun*. **5**, 3876 (2014).

[85] F. Zhang, J. Jung, G. A. Fiete, Q. Niu, and A. H. MacDonald, *Phys. Rev. Lett*. **106**, 156801 (2011).

[86] J. Jung, F. Zhang, Z. Qiao, and A. H. MacDonald, *Phys. Rev. B* **84**, 075418 (2011).

[87] M. Ezawa, *Phys. Rev. B* **88**, 161406 (2013).

[88] J. Lee, K. F. Mak, and J. Shan, arXiv:1508.03068 (2015).

[89] K. F. Mak, K. L. McGill, J. Park, and P. L. McEuen, *Science* **344**, 1489 (2014).

[90] A. F. Morpurgo, private communications.

[91] H. Yu, Y. Wu, G.-B. Liu, X. Xu, and W. Yao, *Phys. Rev. Lett*. **113**, 156603 (2014).

[92] B. W. H. Baugher, H. O. H. Churchill, Y. Yang, and P. Jarillo-Herrero, *Nano Lett*. **13**, 4212 (2013).

[93] X. Cui *et al.*, *Nature Nanotech*. **10**, 534 (2015).

[94] T. Jiang, H. Liu, D. Huang, S. Zhang, Y. Li, X. Gong, Y.-R. Shen, W.-T. Liu, and S. Wu, *Nature Nanotech*. **9**, 825 (2014).

[95] R. Suzuki *et al.*, *Nature Nanotech*. **9**, 611 (2014).

[96] Z. Gong, G.-B. Liu, H. Yu, D. Xiao, X. Cui, X. Xu, and W. Yao, *Nat. Commun*. **4**, 2053 (2013).

[97] A. M. Jones, H. Yu, J. S. Ross, P. Klement, N. J. Ghimire, J. Yan, D. G. Mandrus, W. Yao, and X. Xu, *Nature Phys*. **10**, 130 (2014).

[98] B. Zhu, H. Zeng, J. Dai, Z. Gong, and X. Cui, *Proc. Natl. Acad. Sci. USA* **111**, 11606 (2014).

[99] S. Wu *et al.*, *Nature Phys*. **9**, 149 (2013).